Journal of the Physical Society of Japan **84**, 054402 (2015)
http://dx.doi.org/10.7566/JPSJ.84.054402

# Stable High-Dimensional Spatial Optical Solitons and Vortices in an Active Raman Gain Medium

Hui-jun Li[1,3], Yu-hua Duan[1], Wen Wen[2], and Guoxiang Huang[3]

[1]*Institute of Nonlinear Physics and Department of Physics, Zhejiang Normal University, Jinhua, Zhejiang 321004, China*
[2]*Department of Mathematics and Physics, Hohai University, Changzhou Campus, Changzhou 213022, China*
[3]*State Key Laboratory of Precision Spectroscopy, East China Normal University, Shanghai 200062, China*

(Received December 24, 2014; accepted March 5, 2015; published online April 9, 2015)

We propose a scheme to produce stable high-dimensional spatial optical solitons and vortices in an *M*-type five-level active Raman gain medium at room temperature. We derive a (2+1)-dimensional [(2+1)D] nonlinear Schrödinger (NLS) equation with a 2D trapping potential, which is contributed by an assisted field. We show that by adjusting the system parameter, the signs of the Kerr nonlinearity and the external potential can be manipulated at will. We then present three types of NLS equation, provide their soliton solutions, and analyze their stabilities. We finally discuss the differences in the soliton solutions between (2+1)D and (3+1)D systems with the same 2D trapping potential.

## 1. Introduction

Spatial optical solitons, which occur as a result of the interplay between diffraction and nonlinearity, have been a subject of intensive theoretical and experimental studies for many years. These nonlinear optical wave packets are of special interest owing to their rich nonlinear physics and important practical applications.[1–3] However, up to now, most spatial optical solitons are generated in passive optical media, in which far-off resonance excitation schemes are employed in order to avoid significant optical absorption. In addition, a very high light intensity is used to obtain sufficient nonlinearity for balancing the diffraction effect.

In recent years, much interest has focused on wave propagation in highly resonant optical media via electromagnetically induced transparency (EIT), a typical quantum interference effect occurring in multi-level atomic systems. EIT can be used not only to suppress optical absorption and acquire ultraslow group velocity, but also to enhance Kerr nonlinearity[4] and hence produce temporal,[5–7] spatial[8–12] optical solitons, and even spatiotemporal light bullets.[13]

Parallel to the study of EIT, optical excitations in multi-level atomic systems working on the condition of active Raman gain (ARG) have also been explored. Contrary to the EIT-based scheme that is absorptive in nature, absorption of the signal field in an ARG system can be completely eliminated and a superluminal propagation of the signal field can be realized.[14–18] Research activities on the nonlinear effects in ARG systems have also appeared. In particular, the gain-assisted giant Kerr effect[19] and temporal,[20,21] spatial,[22] and spatiotemporal optical solitons[23] have been shown possible in ARG systems recently.

In this work, we propose a scheme to generate high-D spatial optical solitons and vortices in an *M*-type ARG system. We derive a high-D Ginzburg–Landau (GL) equation with a trapped potential, which is contributed by an assisted field. Owing to the quantum interference effect induced by a control field, the imaginary part in the coefficients of the GL equation can be made much smaller than their corresponding real part. As a result, the GL equation is reduced to a nonlinear Schrödinger (NLS) equation, which allows solutions of gain-assisted high-D nonlinear localized structures (spatial optical solitons and vortices).

The optical solitons and vortices predicted here possess many novel features: (i) They can be actively controlled and manipulated on the basis of the active characters of the system. In particular, the signs of Kerr nonlinearity and external potential can be manipulated at will. As a result, we can construct four different types of NLS equation, some of them have not been investigated so far. (ii) They can be stabilized easily by the assisted field, which provides an external potential acting on the spatial solitons and vortices. Hence, the high-D nonlinear localized structures found here are very robust. (iii) Compared with those solitons and vortices in a 3D system studied in Refs. 13 and 23, they possess many different features, including their spatial profiles, existence domains, and stable domains. Such spatial optical solitons and vortices may have potential applications in optical information processing and transmission.

The rest of the article is arranged as follows. In Sect. 2, we give a simple introduction of the model under study and derive the NLS equation with a trapping potential. In Sect. 3, we investigate the formation and propagation of high-D spatial optical solitons and vortices, and discuss their stability. The final section (Sect. 4) contains a discussion and summary of the main results of our work.

## 2. Model and a High-D NLS Equation

### *2.1 Model*

The model under consideration is a cold, lifetime-broadened atomic gas with an *M*-type level configuration, as shown in Fig. 1. The levels are taken from the $D_1$ line of $^{87}$Rb atoms, with $|1\rangle = |5S_{1/2}, F = 1, m_F = -1\rangle$, $|2\rangle = |5P_{1/2}, F = 1, m_F = -1\rangle$, $|3\rangle = |5S_{1/2}, F = 2, m_F = -2\rangle$, $|4\rangle = |5P_{1/2}, F = 2, m_F = -1\rangle$, and $|5\rangle = |5S_{1/2}, F = 2, m_F = -1\rangle$.

A strong continuous-wave (CW) pump field $\mathbf{E}_p = \mathbf{e}_p\mathcal{E}_p \exp[i(k_p z - \omega_p t)] + \text{c.c.}$ and a weak signal field $\mathbf{E}_s = \mathbf{e}_s\mathcal{E}_s(x, y, z) \exp[i(k_s z - \omega_s t)] + \text{c.c.}$ interact resonantly with levels $|1\rangle \to |3\rangle$ and $|2\rangle \to |3\rangle$, respectively. Here, $\mathbf{e}_j$ and $k_j$ ($\mathcal{E}_j$) are respectively the polarization unit vector in the $j$th direction and the wave number (envelope) of the $j$th field. The levels $|l\rangle$ ($l = 1, 2, 3$) together with $\mathbf{E}_p$ and $\mathbf{E}_s$ constitute a well-known $\Lambda$-type ARG core.

In addition, we use the strong CW control field $\mathbf{E}_c = \mathbf{e}_c\mathcal{E}_c \exp[i(k_c z - \omega_c t)] + \text{c.c.}$ coupling the levels $|2\rangle \to |4\rangle$ to

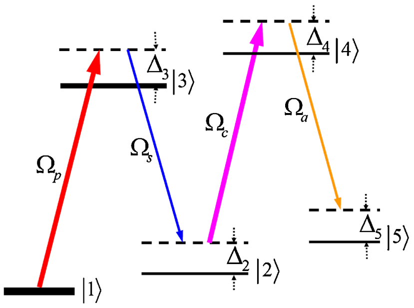


**Fig. 1.** (Color online) (a) Excitation scheme of lifetime-broadened five-state atomic system interacting with a strong pump field (with half Rabi frequency $\Omega_p$), a strong control field (with half Rabi frequency $\Omega_c$), a weak signal field (with half Rabi frequency $\Omega_s$), and a weak assisted field (with half Rabi frequency $\Omega_a$). $\Delta_3$, $\Delta_2$, $\Delta_4$, and $\Delta_5$ are one-photon, two-photon, three-photon, and four-photon detunings, respectively.

suppress the gain of the signal field, and another weak assisted field

$$\begin{aligned}\mathbf{E}_a &= \mathbf{e}_a\mathcal{E}_a(x,y)\exp[i(k_a z-\omega_a t)]+\text{c.c.}\\ &= \mathbf{e}_a\mathcal{E}_{a0}J_l(\sqrt{2(x^2+y^2)/R_\perp^2})\exp[i(k_a z-\omega_a t)]+\text{c.c.}\end{aligned} \tag{1}$$

coupling the levels $|5\rangle \to |4\rangle$ to contribute a trapping potential to the signal field envelope. Here, $J_l$ is the $l$-th order Bessel function, $R_\perp$ is a typical beam radius, and $\mathcal{E}_{a0}$ is a typical amplitude of the assisted field. For simplicity, we assume that all four laser beams propagate along the $z$-axis, and the control and signal fields have large detunings.

Under the electric-dipole and rotating-wave approximations, the Hamiltonian of the system in the interaction picture reads

$$\begin{aligned}\hat{H}_{int} = &-\hbar\sum_{j=1}^{4}\Delta_j|j\rangle\langle j| - \hbar(\Omega_p|3\rangle\langle 1| + \Omega_s|3\rangle\langle 2| + \Omega_c|4\rangle\langle 2|\\ &+ \Omega_a|4\rangle\langle 5| + \text{h.c.}),\end{aligned} \tag{2}$$

where $\Omega_p \equiv (\mathbf{e}_p\cdot\mathbf{p}_{13})\mathcal{E}_p/\hbar$, $\Omega_s \equiv (\mathbf{e}_s\cdot\mathbf{p}_{23})\mathcal{E}_s/\hbar$, $\Omega_c \equiv (\mathbf{e}_c\cdot\mathbf{p}_{24})\mathcal{E}_c/\hbar$, and $\Omega_a \equiv (\mathbf{e}_a\cdot\mathbf{p}_{54})\mathcal{E}_a/\hbar = \Omega_{a0}J_l(\sqrt{2(x^2+y^2)/R_\perp^2})$ are respectively the half Rabi frequencies of pump, signal, control, and assisted fields. $\Delta_3$, $\Delta_2$, $\Delta_4$, and $\Delta_5$ are one-, two-, three-, and four-photon detunings, respectively, and $\Omega_{a0}$ is the typical half Rabi frequency of the assisted field.

The equations of motion for the atomic system and electric field are

$$\left(i\frac{\partial}{\partial t}+d_2\right)A_2 + \Omega_s^* A_3 + \Omega_c^* A_4 = 0, \tag{3a}$$

$$\left(i\frac{\partial}{\partial t}+d_3\right)A_3 + \Omega_p A_1 + \Omega_s A_2 = 0, \tag{3b}$$

$$\left(i\frac{\partial}{\partial t}+d_4\right)A_4 + \Omega_c A_2 + \Omega_a A_5 = 0, \tag{3c}$$

$$\left(i\frac{\partial}{\partial t}+d_5\right)A_5 + \Omega_a^* A_4 = 0, \tag{3d}$$

$$i\left(\frac{\partial}{\partial z}+\frac{1}{c}\frac{\partial}{\partial t}\right)\Omega_s + \frac{c}{2\omega_s}\left(\frac{\partial^2}{\partial x^2}+\frac{\partial^2}{\partial y^2}\right)\Omega_s + \kappa_{23}A_3A_2^* = 0, \tag{3e}$$

with $\sum_{j=1}^{5}|A_j|^2 = 1$, where $d_j \equiv \Delta_j + i\gamma_j$ ($j = 2$ to 5), and $\gamma_j$ is the decay rate of the state $|j\rangle$, $\kappa_{23} = N\omega_s|\mathbf{e}_s\cdot\mathbf{p}_{23}|^2/(2\epsilon_0\hbar c)$, with $N$ being the atomic concentration. The base state (i.e., the steady state of the system when the signal field is absent) is given by $A_1 = 1/\sqrt{1+|\Omega_p|^2/|d_3|^2}$, $A_2 = A_4 = A_5 = 0$, and $A_3 = -(\Omega_p/d_3)A_1$.

### 2.2 *Asymptotic expansion and a high-D NLS equation*

We focus on the steady-state regime of the system, in which time derivative terms in Eq. (3) (and hence the dispersion effect of the system) can be neglected. Such regime can be realized by using the signal field with a large time length (i.e., $|d_{ij}|\tau_0 \gg 1$, where $\tau_0$ is the pulse length of the signal field), and hence the response of atoms can follow the variation of the signal field adiabatically.

Since it is difficult to solve Eq. (3), we apply a singular perturbation method. We firstly derive the nonlinear envelope equation that describes the evolution of the signal field envelope by employing the standard method of multiple scales. Specifically, we make the asymptotic expansions $A_j = \sum_{l=0}^{\infty}\epsilon^l A_j^{(l)}$, $\Omega_s = \sum_{l=1}^{\infty}\epsilon^l\Omega_s^{(l)}$, $\Omega_{a0} = \epsilon\Omega_{a0}^{(1)}$, where $\epsilon$ is a small parameter characterizing the amplitude of the signal field. To obtain a divergence-free expansion, all quantities on the right-hand side of the asymptotic expansions are considered as the functions of the multi-scale variables $z_l = \epsilon^l z$ ($l = 0, 2$) and $(x_1, y_1) = \epsilon(x, y)$. Substituting these expansions and the multi-scale variables into Eq. (3), we obtain a series of linear but inhomogeneous equations for $A_j^{(l)}$ and $\Omega_s^{(l)}$.

At the zeroth order, one can obtain the base state $A_j^{(0)}$ ($j = 1$ to 5) as above. At the first order, the linear solutions are given by

$$\Omega_s^{(1)} = F\,e^{i\theta}, \tag{4a}$$

$$A_2^{(1)} = \frac{d_4A_3^{(0)}}{D}F^*e^{-i\theta^*}, \tag{4b}$$

$$A_4^{(1)} = -\frac{\Omega_cA_3^{(0)}}{D}F^*e^{-i\theta^*}, \tag{4c}$$

with $A_1^{(1)} = A_3^{(1)} = A_5^{(1)} = 0$. Here, $D \equiv |\Omega_c|^2 - d_2d_4$, $\theta \equiv Kz_0$ with $K = \kappa_{23}d_4^{*(0)}|A_3^{(0)}|^2/D^*$, $F$ is the envelope function depending on slow variables $z_2$, $x_1$, and $y_1$, and is to be determined in following. Though $K$ is complex, we can neglect its imaginary part indicating the gain due to the quantum coherent effect induced by the control field.

At $\epsilon^3$ order, using the solvable condition for $\Omega_s^{(3)}$, we obtain the (2+1)D GL equation

$$\begin{aligned}i\frac{\partial}{\partial z_2}F + \frac{c}{2\omega_s}\left(\frac{\partial^2}{\partial x_1^2}+\frac{\partial^2}{\partial y_1^2}\right)F + \alpha_{11}|F|^2F&\\ + \alpha_{12}|\Omega_{a0}^{(1)}J_l|^2F = 0,&\end{aligned} \tag{5}$$

where

$$\begin{aligned}\alpha_{11} = \kappa_{23}\Bigg[&-\frac{|d_4|^2}{d_3|D|^2} - \frac{(d_4^*)^2}{d_3^*(D^*)^2} + \frac{d_4^*|A_3^{(0)}|^2}{D^*}\left(\frac{d_4}{d_3D}+\frac{d_4^*}{d_3^*D^*}\right.\\ &\left.-\frac{|d_4|^2+|\Omega_c|^2}{|D|^2}\right)\Bigg]|A_3^{(0)}|^2,\\ \alpha_{12} = -&\frac{\kappa_{23}|\Omega_cA_3^{(0)}|^2}{d_5^*(D^*)^2}.\end{aligned}$$

After returning to original variables, the (2+1)D GL equation Eq. (5) satisfied by the signal field envelope takes the dimensionless form

 

$$i\frac{\partial u}{\partial s}+\frac{1}{2}\left(\frac{\partial^2}{\partial\xi^2}+\frac{\partial^2}{\partial\eta^2}\right)u+\sigma_1|u|^2u+\sigma_2c_1^2|J_l(\sqrt{2}r)|^2u=0, \tag{6}$$

with $u\equiv\Omega_s/U_0$, $s\equiv z/L_{\rm diff}$, $(\xi,\eta)=(x,y)/R_\perp$, $\sigma_1\equiv\alpha_{11}/|\alpha_{11}|$, $\sigma_2\equiv\alpha_{12}/|\alpha_{11}|$, $c_1=\Omega_{a0}/U_0$, and $r=\sqrt{\xi^2+\eta^2}$. Here, $L_{\rm diff}\equiv\omega_sR_\perp^2/c$ is a typical diffraction length, and we have taken $L_{\rm diff}=L_{NL}$ [$L_{NL}=1/(|\alpha_{11}U_0^2|)$ being a typical nonlinear length], that is, $U_0=\sqrt{c/(\omega_sR_\perp^2|\alpha_{11}|)}$ (typical Rabi frequency of the signal field). Note that $c_1$ is proportional to a typical Rabi frequency of the assisted field $\Omega_{a0}$, which is a free parameter that can be used to control the magnitude of the last term of Eq. (6). It is obvious that the assisted field will contribute an external potential to the signal field.

Because the system under study is an active and lifetime-broadened one, the coefficients in Eq. (6) are generally complex. If the control-field half Rabi frequency $\Omega_c$ is small, the imaginary parts of the coefficients are comparable to their real parts, and hence stable nonlinear excitations do not exist. However, it is easy to show that under the ARG condition $|\Omega_c|^2\gg\gamma_2\gamma_4$, the gain of the signal field can be largely suppressed owing to the quantum interference effect induced by the control field, and thus the imaginary parts of these coefficients can be made to be much smaller than their real parts.[23]

After considering the quantum interference effect induced by the control field, Eq. (6) is reduced to a (2+1)D NLS equation. To estimate the values of the coefficients appearing in the dimensionless NLS equation Eq. (6), we consider a typical warm atomic vapor of $^{87}$Rb[24] with the parameters given by

$$\gamma_1=\Delta_2=0\,\text{Hz},\quad 2\gamma_{2,5}=300\,\text{Hz},$$
$$2\gamma_{3,4}=36\,\text{MHz},\quad \kappa_{23}=3.0\times10^9\,\text{cm}^{-1}\,\text{s}^{-1},$$
$$\omega_s=2.37\times10^{15}\,\text{s}^{-1},\quad R_\perp=3.6\times10^{-3}\,\text{cm},$$
$$\Omega_p=0.75\Omega_c=6.0\times10^7\,\text{s}^{-1}.$$

Other (adjustable) parameters are chosen as follows:

**Case (1).** $\Delta_4=3.75\Delta_3=-3.0\times10^9\,\text{s}^{-1}$, $\Delta_5=-1.4\times10^5\,\text{s}^{-1}$. With these parameters, we obtain

$$\sigma_1=1.0+0.006i,\quad \sigma_2=1.0-0.001i.$$

**Case (2).** $\Delta_4=3.75\Delta_3=-3.0\times10^9\,\text{s}^{-1}$, $\Delta_5=1.4\times10^5\,\text{s}^{-1}$. With these parameters, we obtain

$$\sigma_1=1.0+0.006i,\quad \sigma_2=-1.0+0.001i.$$

**Case (3).** $\Delta_4=3.75\Delta_3=3.0\times10^9\,\text{s}^{-1}$, $\Delta_5=-1.4\times10^5\,\text{s}^{-1}$. With these parameters, we obtain

$$\sigma_1=-1.0-0.006i,\quad \sigma_2=1.0-0.001i.$$

**Case (4).** $\Delta_4=3.75\Delta_3=3.0\times10^9\,\text{s}^{-1}$, $\Delta_5=1.4\times10^5\,\text{s}^{-1}$. With these parameters, we obtain

$$\sigma_1=-1.0-0.006i,\quad \sigma_2=-1.0+0.001i,$$

with $L_D=1.0\,\text{cm}$, $U_0=7.2\times10^6\,\text{s}^{-1}$.

It is obvious that the signs of the Kerr nonlinearity coefficient $\sigma_1$ and the external potential coefficient $\sigma_2$ can be manipulated by adjusting the detunings $\Delta_3$, $\Delta_4$, and $\Delta_5$. Cases 1 and 2 correspond to the self-focusing models, and Cases 3 and 4 are for the self-defocusing models. We see that the imaginary part of $\sigma_{1,2}$ is much less than its real part, and hence can be taken as a small perturbation. For Case (4), we do not find its soliton solution.

## 3. High-D Spatial Optical Solitons and Vortices

We now investigate the possibilities of spatial optical solitons and vortices supported by Kerr nonlinearity, on the basis of the NLS equation Eq. (6). Equation (6) admits several conserved quantities, including the power, $P=2\pi\int_0^\infty r|u|^2dr$.

Using the transformation $u=\psi(r)\exp[i\mu s+im\phi]$, Eq. (6) becomes

$$\frac{\partial^2\psi}{\partial r^2}+\frac{1}{r}\frac{\partial\psi}{\partial r}-\frac{m^2}{r^2}\psi-2\mu\psi+2\sigma_1\psi^3 + 2c_1^2\sigma_2|J_l(\sqrt{2}r)|^2\psi=0, \tag{7}$$

where $m\geq0$ is an integer vorticity and $\mu$ is the propagation constant. For $m\neq0$, the beam hosts a vortex of topological charge $m$. Boundary conditions are $\partial\psi/\partial r=0$ at $r=0$ and $\psi=0$ at $r\to\infty$ for $m=0$ (for solitons), or $\psi=0$ at $r=0$ and $r\to\infty$ for $m>0$ (for vortices). The stable solitons and vortices are shown in the following subsection.

The stability of the soliton can be analyzed by considering the perturbed stationary solution form as

$$u(\xi,\eta,s)=[\psi(r)+\varepsilon'w_1(r)\exp(i\lambda s+in\phi) + \varepsilon'w_2(r)\exp(-i\lambda s-in\phi)]\exp(i\mu s+im\phi),$$

where the perturbation components $w_1$ and $w_2$ are real functions and grow with the complex rate $\lambda$ during propagation; $n$ is the azimuthal index. The soliton (or vortex) is stable if the imaginary part of the perturbation eigenvalue $\lambda$ is equal to zero. By substituting the perturbed solution into Eq. (6), the first order equations of $\varepsilon'$ are the eigenequations

$$\begin{aligned}\lambda w_1&=\frac{1}{2}\left[\frac{\partial^2}{\partial r^2}+\frac{1}{r}\frac{\partial}{\partial r}-\frac{(m+n)^2}{r^2}\right]w_1-\mu w_1\\&\quad+\sigma_1(2w_1+w_2)\psi^2+\sigma_2c_1^2|J_l(\sqrt{2}r)|^2w_1,\\ \lambda w_2&=-\frac{1}{2}\left[\frac{\partial^2}{\partial r^2}+\frac{1}{r}\frac{\partial}{\partial r}-\frac{(m-n)^2}{r^2}\right]w_2+\mu w_2\\&\quad-\sigma_1(2w_2+w_1)\psi^2-\sigma_2c_1^2|J_l(\sqrt{2}r)|^2w_2,\end{aligned} \tag{8}$$

which can be solved numerically.

### 3.1 *Results for Eq. (6) with $\sigma_1=1$, $\sigma_2=1$*

In this subsection, we will discuss the soliton and vortex solutions, their evolutions and stability for Eq. (6) with $\sigma_1=1$ and $\sigma_2=1$.

The fundamental soliton solutions and rotary soliton solutions of this model with the zero-order Bessel external potential $J_0(\sqrt{20}r)$ have been discussed in Ref. 25, but the external potential is the first power of the zero-order Bessel function. We will show the fundamental soliton solutions and vortex solutions trapped by the zero- and first-order Bessel potentials (the second power of the Bessel function, that is, $|J_l(\sqrt{2}r)|^2$, $l=0,1$) in Figs. 2–5.

In Fig. 2, we discuss the fundamental soliton solutions of Eq. (6) with the zero-order Bessel potential $|J_0(\sqrt{2}r)|^2$. The power curves with propagation constant are given in Fig. 2(a). These monotonically increasing curves not only tell us the existence domain of the fundamental solitons, but also

 

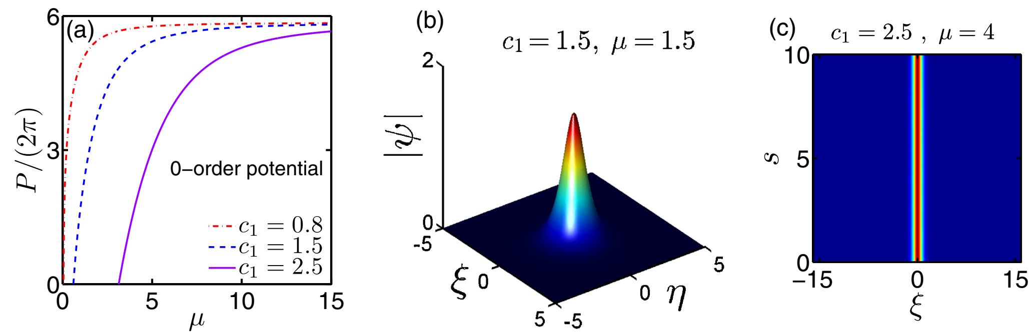


**Fig. 2.** (Color online) Results of fundamental solitons for Eq. (6) with $\sigma_1 = 1$, $\sigma_2 = 1$ and zero-order Bessel potential. (a) Power of fundamental soliton versus propagation constant. (b) Soliton profile $|\psi|$ with $c_1 = 1.5$, $\mu = 1.5$. (c) Propagation of fundamental soliton with $c_1 = 2.5$, $\mu = 4$ in the presence of the perturbation.

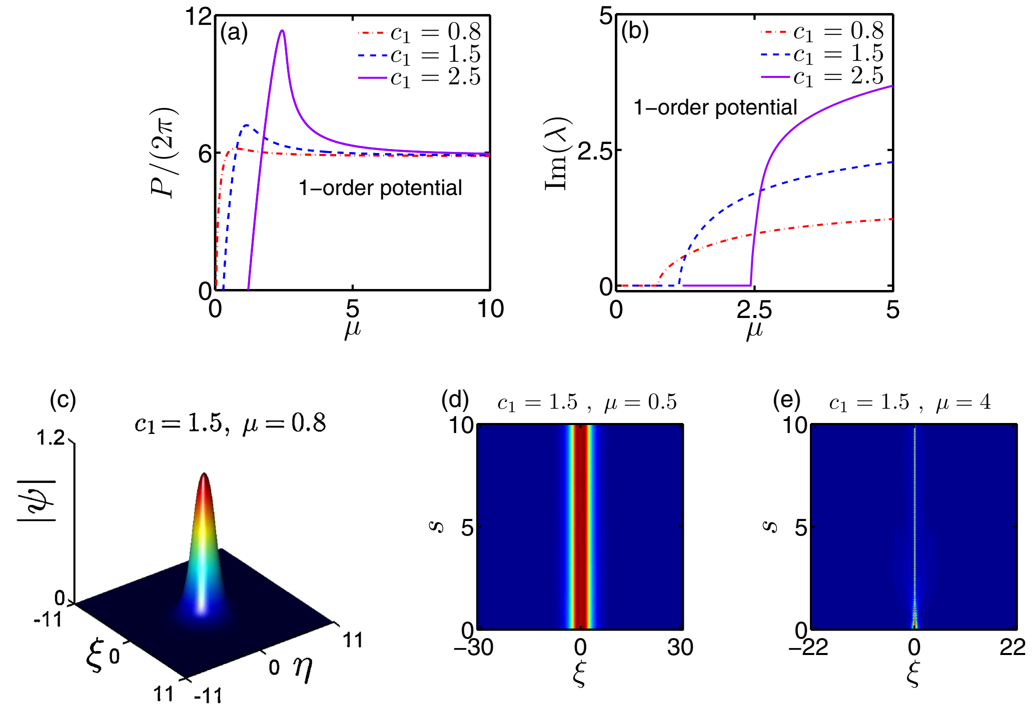


**Fig. 3.** (Color online) Results of fundamental solitons for Eq. (6) with $\sigma_1 = 1$, $\sigma_2 = 1$ and the first-order Bessel potential. (a) Power of fundamental soliton versus propagation constant. (b) Perturbation growth rate versus propagation constant. (c) Soliton profile $|\psi|$ with $c_1 = 1.5$, $\mu = 0.8$. Propagations of fundamental soliton with $c_1 = 1.5$, $\mu = 0.5$ in (d) and $c_1 = 1.5$, $\mu = 4$ in (e). The random perturbation distributed in the interval $[0, 0.1]$ is added into the initial condition.

show the stable domain ($dP/d\mu > 0$) according to Vakhitov–Kolokolov (VK) stability criterion. Through the power curves, we find that the stable domain of the fundamental solitons are the same as the existence domain, and it narrows with the potential depth $c_1$ increasing. And the stability is also proved by solving Eq. (8) of the linear stability analysis. The typical fundamental soliton profile corresponding to $c_1 = 1.5$, $\mu = 1.5$ is shown in Fig. 2(b). To confirm the results of the linear stability analysis and the conclusion of VK criterion, propagation of a fundamental soliton solution with $c_1 = 2.5$, $\mu = 4$ is carried out by numerical solving Eq. (6) with the perturbed initial condition $u(s = 0, \xi, \eta) = \psi(\xi, \eta)(1 + \varepsilon'' f)$ in Fig. 2(c). Here, $\varepsilon'' = 0.1$ is a typical amplitude of the perturbation, and $f$ is a random variable uniformly distributed in the interval $[0, 1]$.

The fundamental soliton solutions of Eq. (6) with the first-order Bessel potential $|J_1(\sqrt{2}r)|^2$ are shown in Fig. 3. From Fig. 3(a), the power curves are not the monotonic function of the propagation constant. With the propagation constant increasing, the power increases firstly, then decreases to a certain value. In Fig. 3(b), the results of the linear stability analysis are shown by solving Eq. (8). It is obvious that the stable domain obtained by the linear stability analysis in Fig. 3(b) is in perfect agree with the domain of $dP/d\beta > 0$ in Fig. 3(a). Moreover, with increasing depth $c_1$, the existence domain narrows, but the stable domain widens. The profile of the soliton corresponding to $c_1 = 1.5$, $\mu = 0.8$ is shown in Fig. 3(c). Propagations of fundamental soliton solutions with $c_1 = 1.5$, $\mu = 0.5$ (located in the stable domain) in Fig. 3(d) and $c_1 = 1.5$, $\mu = 4$ (located in the unstable domain) in Fig. 3(e) are carried out by numerically solving Eq. (6) with the perturbed initial condition. The numerical propagations prove these results of the linear stability analysis and VK stability criterion.

 

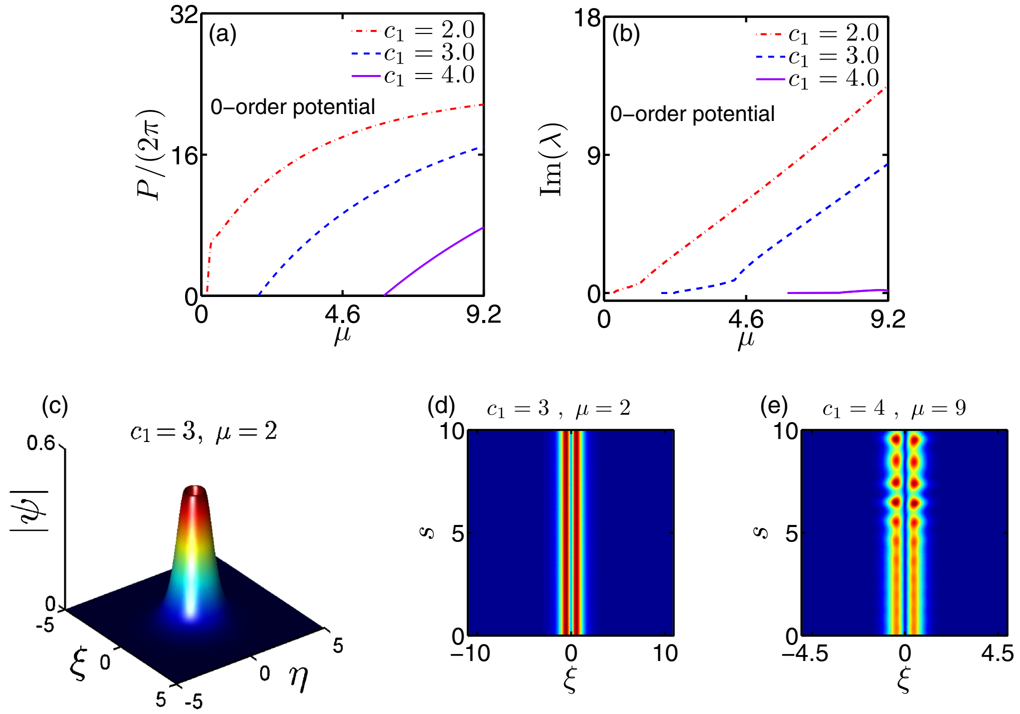


**Fig. 4.** (Color online) Results of vortices ($m = 1$) for Eq. (6) with $\sigma_1 = 1$, $\sigma_2 = 1$ and the zero-order Bessel potential. (a) Power of fundamental soliton versus propagation constant. (b) Perturbation growth rate versus propagation constant. (c) Vortex profile $|\psi|$ with $c_1 = 3$, $\mu = 2$. Propagations of vortices with $c_1 = 3$, $\mu = 2$ in (d) and $c_1 = 4$, $\mu = 9$ in (e). The random perturbation is added into the initial input.

Compared with those results of the (3+1)D model [that is, adding the dispersion term into Eq. (6)],[13] one conclusion, that is, the stable domain of the fundamental soliton trapped by the first-order Bessel potential is narrower than that of the zero-order Bessel potential, is identical for a given $c_1$. However, the trend of the power curves with the propagation constant is completely different, and the stable domain is wider in the present model than in the (3+1)D model.[13]

In Fig. 4, we find the vortex solutions ($m = 1$) of Eq. (6) with the zero-order Bessel potential $|J_0(\sqrt{2}r)|^2$. From Fig. 4(a), the power curves are the monotonically increasing function of the propagation constant. According to these power curves, we can determine the existence domain rather than the stable domain. Here, the VK stability criterion is not applicable. In Fig. 4(b), the results of the linear stability analysis are shown by solving Eq. (8). With increasing depth $c_1$, the existence domain narrows, but the stable domain widens. The profile of the soliton corresponding to $c_1 = 3$, $\mu = 2$ is shown in Fig. 4(c). Propagations of fundamental soliton solutions with $c_1 = 3$, $\mu = 2$ (located in the stable domain) in Fig. 4(d) and $c_1 = 4$, $\mu = 9$ (located in the unstable domain) in Fig. 4(e) are carried out by numerically solving Eq. (6) with the perturbed initial condition. The propagations prove the results of the linear stability analysis.

In Fig. 5, we obtain the vortex solutions ($m = 1$) of Eq. (6) with the first-order Bessel potential $|J_1(\sqrt{2}r)|^2$. In Fig. 5(a), the power curves that determined the existence domain are shown for different $c_1$. In Fig. 5(b), the results of the linear stability analysis are plotted by solving Eq. (8). According to the above results, with increasing depth $c_1$, the existence domain narrows, but the stable domain widens. Compared with those results in Fig. 4, the stable domain of the vortices trapped by the first-order Bessel potential is narrower than that of the zero-order potential. The reason is that the trapping potential becomes weak. The profile of the vortex corresponding to $c_1 = 3$, $\mu = 1.48$ is shown in Fig. 5(c). Propagations of vortex solutions with $c_1 = 4$, $\mu = 3.46$ (located in the stable domain) in Fig. 5(d) and $c_1 = 4$, $\mu = 4.4$ (located in the unstable domain) in Fig. 5(e) are carried out by numerically solving Eq. (6) with the perturbed initial condition.

All these results about vortices are consistent with that of the (3+1)D system.[23]

### 3.2 *Results for Eq. (6) with $\sigma_1 = -1$, $\sigma_2 = 1$*

In this subsection, we will discuss the soliton and vortex solutions, their evolutions and stability for Eq. (6) with $\sigma_1 = -1$, $\sigma_2 = 1$.

It is known that homogeneous defocusing Kerr nonlinear media support the stable dark solitons rather than the stable bright solitons. However, in the confined system, such as graded-index optical fibers, trapped Bose–Einstein condensates, or nonlinear photonic crystals with defects, the stable bright solitons are induced by the corresponding confining potentials. The fundamental solitons, vortices,[26] multipole-mode solitons,[27] necklace solitons, and ring solitons[28] of this model with the first-order Bessel external potential have been discussed, but the case of the zero-order Bessel external potential has not been considered. According to the results of numerical simulation, we find that both the stable and existence domains of solitons and vortices trapped by the first-order Bessel potential are narrower than those trapped by the zero-order potential. In the case of the (3+1)D model trapped by the 2D potential, there are only soliton and vortex train solutions.[23] In following, we will show the fundamental soliton solutions (see Fig. 6) and vortex solutions (see Fig. 7)

 

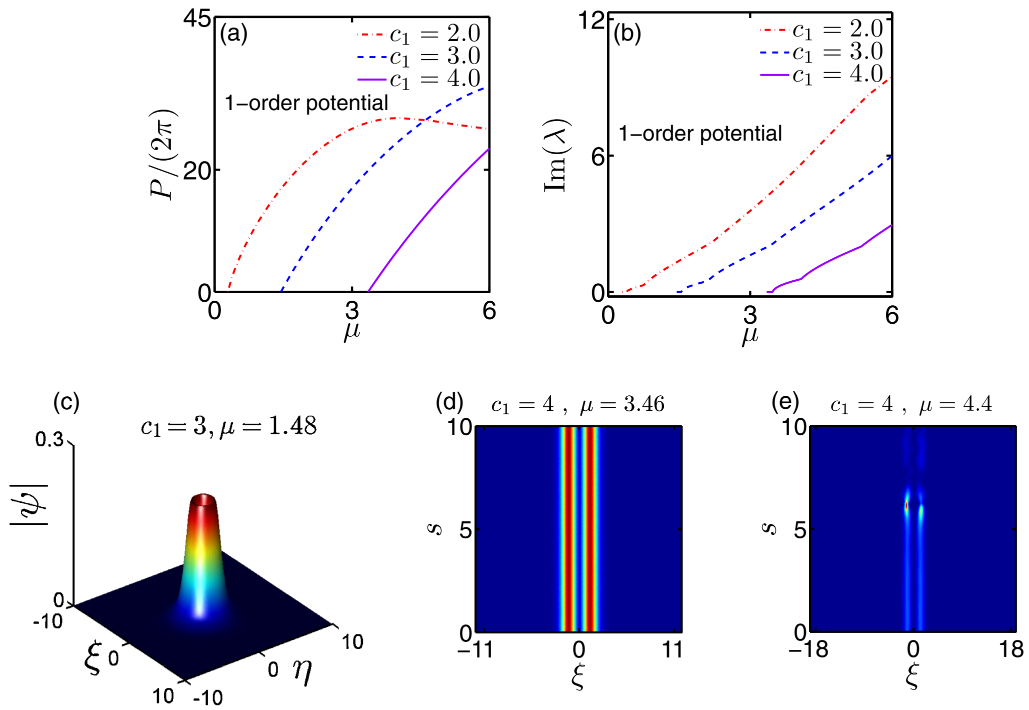


**Fig. 5.** (Color online) Results of vortices ($m = 1$) for Eq. (6) with $\sigma_1 = 1$, $\sigma_2 = 1$ and the first-order Bessel potential. (a) Power of fundamental soliton versus propagation constant. (b) Perturbation growth rate versus propagation constant. (c) Vortex profile $|\psi|$ with $c_1 = 3$, $\mu = 1.48$. Propagations of vortices with $c_1 = 4$, $\mu = 3.46$ in (d) and $c_1 = 4$, $\mu = 4.4$ in (e). The random perturbation is added into the initial condition.

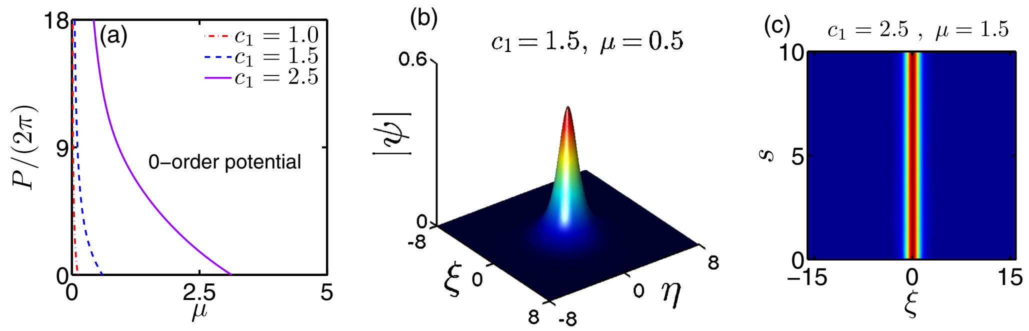


**Fig. 6.** (Color online) Results of fundamental solitons for Eq. (6) with $\sigma_1 = -1$, $\sigma_2 = 1$ and the zero-order Bessel potential. (a) Power of fundamental soliton versus propagation constant. (b) Soliton profile $|\psi|$ with $c_1 = 1.5$, $\mu = 0.5$. (c) Propagation of fundamental soliton with $c_1 = 2.5$, $\mu = 1.5$ in the presence of the perturbation.

trapped by the zero-order Bessel potential. Results of the first-order Bessel potential are not listed here to save space.

In Fig. 6, the fundamental soliton solutions of Eq. (6) with the zero-order Bessel potential $|J_0(\sqrt{2}r)|^2$ are discussed. The monotonically decreasing power curves with propagation constant are given in Fig. 6(a). By solving the eigen-equation Eq. (8), we find that these existence solitons are all stable. It is in agreement with the conclusion of the fundamental soliton solutions trapped by the first-order Bessel potential Ref. 26. The typical fundamental soliton profile corresponding to $c_1 = 1.5$, $\mu = 0.5$ is shown in Fig. 6(b). To confirm the results of the linear stability analysis, the propagation of a fundamental soliton solution with $c_1 = 2.5$, $\mu = 1.5$ is carried out by numerically solving Eq. (6) with the perturbed initial condition.

In Fig. 7, we consider the vortex solutions ($m = 1$) of Eq. (6) with the zero-order Bessel potential $|J_0(\sqrt{2}r)|^2$. From Fig. 7(a), the power curves are the monotonically decreasing function of the propagation constant. According to these power curves, we can determine the existence domain, but the VK stability criterion is not applicable. In Fig. 7(b), the results of the linear stability analysis are shown by solving Eq. (8). The stable domains of the propagation constant $\mu$ are $[0.06, 0.18]$ for $c_1 = 2$, $[1.75, 2.0]$ for $c_1 = 3$, and $[5.67, 5.95]$ for $c_1 = 4$. With the depth $c_1$ increasing, the existence and stable domains both widen. After some further numerical simulations, we find that the existence domain is the same as the stable domain when $c_1 < 2.49$ [as shown by the dotted-dashed line in Fig. 7(b)]. The soliton profile corresponding to $c_1 = 3$, $\mu = 1.85$ is shown in Fig. 7(c). Propagations of fundamental soliton solutions with $c_1 = 4$, $\mu = 5.8$ (located in the stable domain) in Fig. 7(d) and $c_1 = 4$, $\mu = 4$ (located in the unstable domain) in Fig. 7(e) are carried out by numerically solving Eq. (6) with the perturbed initial condition. The propagations prove the results of the linear stability analysis.

 

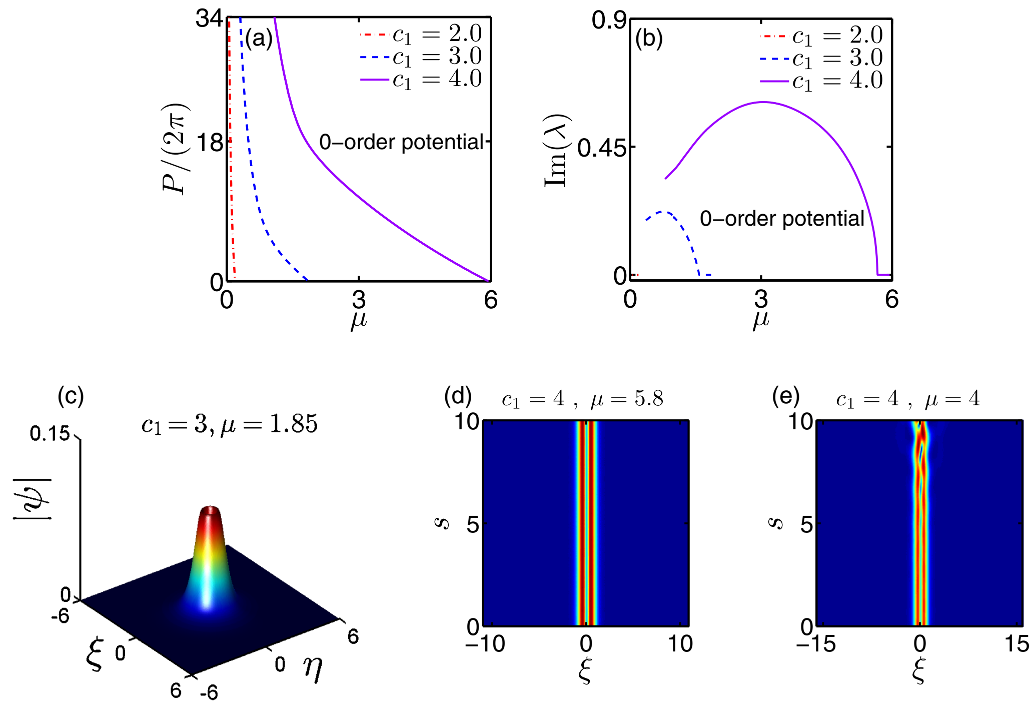


**Fig. 7.** (Color online) Results of vortices ($m = 1$) for Eq. (6) with $\sigma_1 = -1$, $\sigma_2 = 1$ and the zero-order Bessel potential. (a) Power of vortices versus propagation constant. (b) Perturbation growth rate versus propagation constant. (c) Vortex profile $|\psi|$ with $c_1 = 3$, $\mu = 1.85$. Propagations of vortices with $c_1 = 4$, $\mu = 5.8$ in (d) and $c_1 = 4$, $\mu = 4$ in (e). The random perturbation is added into the initial condition.

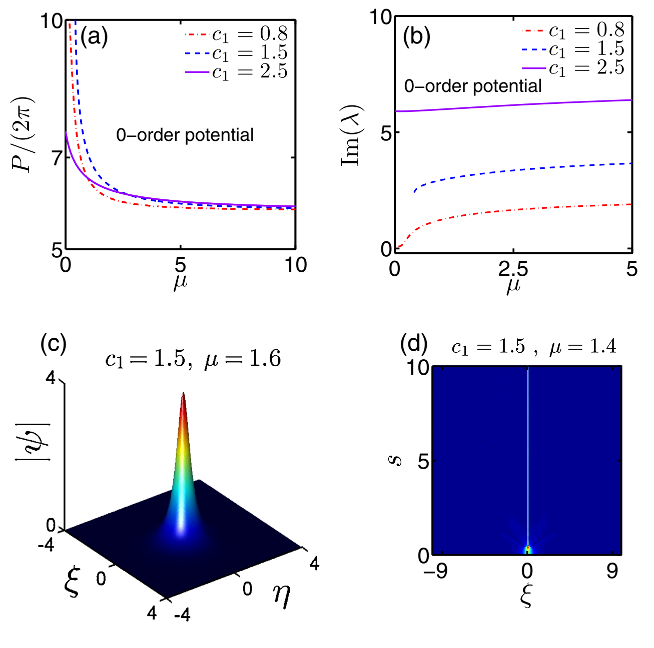


**Fig. 8.** (Color online) Results of solitons for Eq. (6) with $\sigma_1 = 1$, $\sigma_2 = -1$ and the zero-order Bessel potential. (a) Power of fundamental solitons versus propagation constant. (b) Perturbation growth rate versus propagation constant. (c) Fundamental soliton profile $|\psi|$ with $c_1 = 1.5$, $\mu = 1.6$. (d) Propagation of soliton with $c_1 = 1.5$, $\mu = 1.4$. The random perturbation is added into the initial condition.

### *3.3 Results for Eq. (6) with $\sigma_1 = 1$, $\sigma_2 = -1$*

In this subsection, we will discuss the soliton and vortex solutions, their evolutions and stability for Eq. (6) with $\sigma_1 = 1$, $\sigma_2 = -1$.

To the best of our knowledge, the soliton and vortex solutions of the present system have not been reported. Moreover, there are no soliton solutions in the (3+1)D system [adding the dispersion term into Eq. (6)]. In the following, we will show the fundamental soliton solutions trapped by the zero- and first-order Bessel potentials in Figs. 8 and 9, respectively. Although there exist vortex solutions, all of them are unstable. To save space, we do not list them here.

In Fig. 8, the fundamental soliton solutions of Eq. (6) with the zero-order Bessel potential $|J_0(\sqrt{2}r)|^2$ are found. The monotonically decreasing power curves with the propagation constant are shown in Fig. 8(a). According to the VK stability criterion, all of these solitons are unstable. This conclusion is proved by the linear stability analysis in Fig. 8(b). With $c_1$ increasing, the solitons are more unstable. The profile of the soliton corresponding to $c_1 = 1.5$, $\mu = 1.6$ is shown in Fig. 8(c). The propagation of fundamental soliton solution with $c_1 = 1.5$, $\mu = 1.4$ is carried out and shown in Fig. 8(d). It further proves the results of the linear stability analysis.

Fortunately, we find that the fundamental solitons trapped by the first-order Bessel potential are stable (see Fig. 9). In Fig. 9(a), the power curves with the propagation constant are shown. With the propagation constant increasing, the power decreases firstly, then increases to a certain value when $c_1 \le 2.02$. That is, when $c_1 > 2.02$, the power curves are the monotonically increasing function of the propagation constant. According to the VK stability criterion, the stable domain widens with increasing $c_1$, and all the solitons will be stable when $c_1 > 2.02$. The result is proved by the linear stability analysis in Fig. 9(b). The profile of the soliton corresponding to $c_1 = 1.5$, $\mu = 1.5$ is shown in Fig. 9(c). Propagations of fundamental soliton solutions with $c_1 = 2.5$, $\mu = 0.2$ (located in the stable domain) in Fig. 9(d) and $c_1 = 0.8$, $\mu = 0.3$ (located in the unstable domain) in

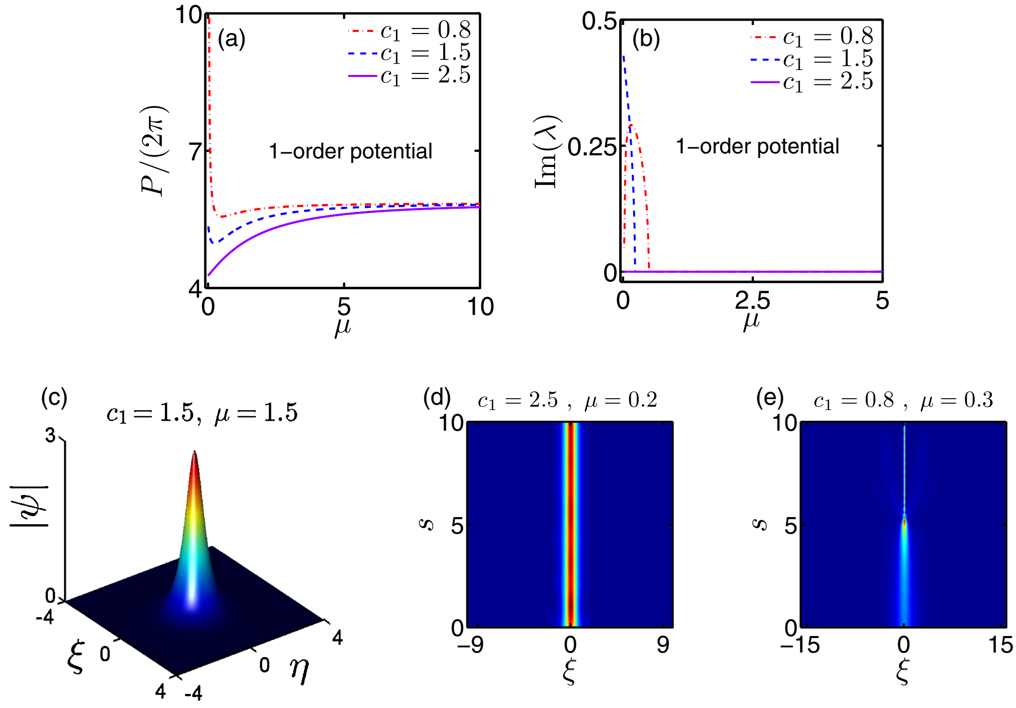


**Fig. 9.** (Color online) Results of fundamental solitons for Eq. (6) with $\sigma_1 = 1$, $\sigma_2 = -1$ and the first-order Bessel potential. (a) Power of fundamental solitons versus propagation constant. (b) Perturbation growth rate versus propagation constant. (c) Soliton profile $|\psi|$ with $c_1 = 1.5$, $\mu = 1.5$. Propagations of solitons with $c_1 = 2.5$, $\mu = 0.2$ in (d) and $c_1 = 0.8$, $\mu = 0.3$ in (e). The random perturbation is added into the initial condition.

Fig. 9(e) are carried out by numerically solving Eq. (6) with the perturbed initial condition.

## 4. Summary

In this article, we have proposed a scheme to generate stable high-D spatial optical solitons and vortices in an $M$-type five-level active Raman gain medium at room temperature. We have derived a (2+1)-dimensional [(2+1)D] NLS equation with a 2D trapping potential, which is contributed by an assisted field. We have shown that by adjusting system parameters, the signs of the Kerr nonlinearity and the linear external potential can be manipulated at will. We have also presented three types of NLS equation, provided their soliton solutions, and analyzed their stability. Finally, we have discussed the differences in the soliton solutions between (2+1)D and (3+1)D models with the same 2D trapping potential. The results presented here are useful for understanding the nonlinear property of coherent atomic systems and guiding experimental findings of spatial solitons and vortices, which may have potential applications in optical information processing and transmission.

## Acknowledgments

This work was supported by the NSF-China under Grant Nos. 11105039, 11175158, and 11204274, and by the Open Fund from the State Key Laboratory of Precision Spectroscopy, ECNU.

1) G. I. Stegeman and M. Segev, Science **286**, 1518 (1999).
2) Y. S. Kivshar and G. P. Agrawal, *Optical Solitons: From Fibers to Photonic Crystals* (Academic Press, New York, 2003).
3) M. J. Paz-Alonso and H. Michinel, Phys. Rev. Lett. **94**, 093901 (2005).
4) M. Fleischhauer, A. Imamoglu, and J. P. Marangos, Rev. Mod. Phys. **77**, 633 (2005), and references therein.
5) Y. Wu and L. Deng, Phys. Rev. Lett. **93**, 143904 (2004).
6) G. Huang, L. Deng, and M. G. Payne, Phys. Rev. E **72**, 016617 (2005).
7) W.-X. Yang, A.-X. Chen, L.-G. Si, K. Jiang, X. Yang, and R.-K. Lee, Phys. Rev. A **81**, 023814 (2010).
8) T. Hong, Phys. Rev. Lett. **90**, 183901 (2003).
9) H. Michinel, M. J. Paz-Alonso, and V. M. Perez-Garcia, Phys. Rev. Lett. **96**, 023903 (2006).
10) C. Hang, G. Huang, and L. Deng, Phys. Rev. E **74**, 046601 (2006).
11) Y. P. Zhang, Z. G. Wang, Z. Q. Nie, C. B. Li, H. X. Chen, K. Q. Lu, and M. Xiao, Phys. Rev. Lett. **106**, 093904 (2011).
12) U. Khadka, J. T. Sheng, and M. Xiao, Phys. Rev. Lett. **111**, 223601 (2013).
13) H. J. Li, Y. P. Wu, and G. X. Huang, Phys. Rev. A **84**, 033816 (2011).
14) See R. Y. Chiao and A. M. Steinberg, in *Progress in Optics*, ed. E. Wolf (Elsevier, Amsterdam, 1997) pp. 345–405, and references therein.
15) L. J. Wang, A. Kuzmich, and A. Dogariu, Nature **406**, 277 (2000).
16) M. S. Bigelow, N. N. Lepeshkin, and R. W. Boyd, Science **301**, 200 (2003).
17) M. D. Stenner, D. J. Gauthier, and M. A. Neifield, Nature **425**, 695 (2003).
18) J. Zhang, G. Hernandez, and Y. Zhu, Opt. Lett. **31**, 2598 (2006).
19) L. Deng and M. G. Payne, Phys. Rev. Lett. **98**, 253902 (2007).
20) G. Huang, C. Hang, and L. Deng, Phys. Rev. A **77**, 011803(R) (2008).
21) H. J. Li, C. Hang, G. Huang, and L. Deng, Phys. Rev. A **78**, 023822 (2008).
22) H. J. Li, L. W. Dong, C. Hang, and G. X. Huang, Phys. Rev. A **83**, 023816 (2011).
23) H. J. Li, Y. P. Wu, C. Hang, and G. X. Huang, Phys. Rev. A **86**, 043829 (2012).
24) D. A. Steck, Rubidium 87 D Line Data [http://steck.us/alkalidata/].
25) Y. V. Kartashov, V. A. Vysloukh, and L. Torner, Phys. Rev. Lett. **93**, 093904 (2004).
26) Y. V. Kartashov, V. A. Vysloukh, and L. Torner, Phys. Rev. Lett. **94**, 043902 (2005).
27) Y. V. Kartashov, R. Carretero-González, B. A. Malomed, V. A. Vysloukh, and L. Torner, Opt. Express **13**, 10703 (2005).
28) L. Dong, H. Wang, W. Zhou, X. Yang, X. Lv, and H. Chen, Opt. Express **16**, 5649 (2008).

 